

Nonparanormal Graph Quilting with Applications to Calcium Imaging

Andersen Chang*¹ Lili Zheng*² Gautam Dasarthy³ Genevera I. Allen^{2,4,5,6}

¹Department of Neuroscience, Baylor College of Medicine

²Department of Electrical and Computer Engineering, Rice University

³School of Electrical, Computer and Energy Engineering, Arizona State University

⁴Department of Computer Science, Rice University

⁵Department of Statistics, Rice University

⁶Jan and Dan Duncan Neurological Research Institute, Texas Children’s Hospital

Abstract

Probabilistic graphical models have become an important unsupervised learning tool for detecting network structures for a variety of problems, including the estimation of functional neuronal connectivity from two-photon calcium imaging data. However, in the context of calcium imaging, technological limitations only allow for partially overlapping layers of neurons in a brain region of interest to be jointly recorded. In this case, graph estimation for the full data requires inference for edge selection when many pairs of neurons have no simultaneous observations. This leads to the Graph Quilting problem, which seeks to estimate a graph in the presence of block-missingness in the empirical covariance matrix. Solutions for the Graph Quilting problem have previously been studied for Gaussian graphical models; however, neural activity data from calcium imaging are often non-Gaussian, thereby requiring a more flexible modeling approach. Thus, in our work, we study two approaches for nonparanormal Graph Quilting based on the Gaussian copula graphical model, namely a maximum likelihood procedure and a low-rank based framework. We provide theoretical guarantees on edge recovery for the former approach under similar conditions to those previously developed for the Gaussian setting, and we investigate the empirical performance of both methods using simulations as well as real data calcium imaging data. Our approaches yield more scientifically meaningful functional connectivity estimates compared to existing Gaussian graph quilting methods for this calcium imaging data set.

Index terms— Graphical models; Graph quilting; Nonparanormal graphical models; Rank-based correlation; Functional connectivity; Covariance completion

1 Introduction

Probabilistic graphical models are a popular unsupervised learning technique for inference and sparse edge selection in network estimation, and are an important tool for understanding dependency structures in high-dimensional data. Graphical modeling approaches have been employed for data analysis in a wide variety of areas, including neuroscience (Yatsenko et al., 2015; Carrillo-Reid et al., 2021; Subramaniyan et al., 2018), genomics (Allen and Liu, 2013; Hartemink et al., 2000), and sensor networks (Chen et al., 2016; Dasarthy et al., 2016). One particular research problem where graphical models are applied is in the study of functional neuronal connectivity, defined as statistical relationships between the activities of neurons in the brain, from two-photon calcium imaging data (Horwitz, 2003; Fingelkurts et al., 2005). Functional neuronal connectivity is of particular interest in the realm of neuroscience as a mechanism for describing how neuronal circuits in the brain are organized and for finding patterns in neuronal activity that underlies how information is passed between different regions of the brain (Feldt et al., 2011); it may also serve well as a proxy for deriving the structural synaptic connectivity between individual neurons in the brain, as well as provide insight into the relationship between the two (Deco et al., 2014).

*Co-first authors on this manuscript.

Due to technological limitations, in many calcium imaging experiments, the full set of neurons in a brain region of interest are never simultaneously observed. Instead, scans of functional activity are recorded in sequential, partially overlapping layers, each containing only a subset of the population of neurons (Grienberger and Konnerth, 2012; Berens et al., 2017; Pnevmatikakis et al., 2016). This data collection scheme leads to block-missingness in the ensuing computation of the empirical covariance matrix for the functional recording data on all neurons, as the joint activity of many pairs are never observed; we demonstrate this visually in Figures 1a and 1b. Therefore, in order to estimate a graphical model for functional neuronal connectivity for the full set of observed neurons, the edge structure in the missing portion must be inferred using the information from the existing contemporaneous joint observations. The estimation of a graph in the presence of block missing entries in the covariance matrix is known as the Graph Quilting problem (Vinci et al., 2019).

Previously, several approaches have been developed in order to address the Graph Quilting problem. (Vinci et al., 2019) originally proposed the Maximum Determinant (MAD_{GQ}) algorithm, which first finds an ℓ_1 -regularized maximum likelihood estimate of the graph on the observed portion of the covariance matrix with the constraint that no edges are affiliated with unobserved elements, then applies thresholding and Schur complements on the result in order to identify graph edges and a minimal superset of edges. Later, (Chang et al., 2022) introduced the Low Rank Graph Quilting (LRGQ) approach, which utilizes a two-step procedure of covariance imputation under the assumption of the existence of a low-rank representation of the underlying covariance matrix, followed by the application of the graphical Lasso. Both of the aforementioned Graph Quilting procedures have shown positive results for graph imputation and edge recovery in the presence of block-wise missingness in the entries of the full covariance matrices. However, their scope is currently restricted to the case where the full underlying data follow a multivariate Gaussian distribution. In particular, as the sample covariance is the sufficient statistic for Gaussian graphical models, these methods and their theory are both developed with a focus on accurately estimating or imputing the covariance in the Gaussian setting. The empirical studies in these papers for validating their methods also focused only on data fit to standard Gaussian graphical models. Another related work, (Massa and Chiogna, 2013), also proposes and empirically studies an approach of combining multiple graphical models of subsets of variables to a full graph, which are in similar spirit to the MAD_{GQ} algorithm in (Vinci et al., 2019), with a focus on the Gaussian setting.

Functional activity data from calcium imaging, on the other hand, tends to be highly non-Gaussian. In particular, as shown in Figures 1c and 1d, the distribution of the fluorescence traces, which represent the firing activity of each individual neuron from calcium imaging data, is heavily right skewed with extreme positive outliers. To address this problem in the realm of graphical models, approaches which assume that the data follow a parametric distribution other than the Gaussian have been developed. For example, many have explored elliptical distributions (Vogel and Fried, 2011; Finegold and Drton, 2011) and general exponential family distributions (Yang et al., 2015, 2018) when the Gaussian assumption may not be appropriate. For the specific case of estimating functional neuronal connectivity, the most common alternative to a Gaussian-based method is the Poisson graphical model (Yang et al., 2013), which assumes that the number of spikes of each neuron across time bins follows a Poisson distribution (Xue et al., 2014; Vinci et al., 2018). The Poisson distribution is also the basis for a variety of other approaches for estimating functional connectivity outside of the graphical modeling paradigm, such as the linear-nonlinear model (Pillow et al., 2008; Stevenson et al., 2008) and time series modeling with inter-spike intervals (Masud and Borisyuk, 2011). More recently, (Chang and Allen, 2021) proposed a different class of graphical models specifically for functional neuronal connectivity based on the Subbotin distribution in order to capture conditional dependencies between extreme values in the activity traces, which directly represent neuronal activity. Nonlinear correlation methods, which employ information theory metrics such as mutual information and joint entropy, have also been used to derive functional neuronal connectivity from calcium imaging data (Garofalo et al., 2009; Stetter et al., 2012).

While the aforementioned non-Gaussian functional neuronal connectivity models have shown encouraging results for the calcium imaging application, they may not be naturally suitable for the Graph Quilting problem. In order to leverage existing ideas (Vinci et al., 2019; Chang et al., 2022) for solving this problem, we still hope to operate on some pairwise similarity matrix like the empirical covariance calculated from the observations rather than the raw data itself. Therefore, we consider one particular alternative to the Gaussian graphical model that can be applied to the Graph Quilting problem in the non-Gaussian setting and which has been used for the analysis of functional neuronal connectivity from calcium imaging data:

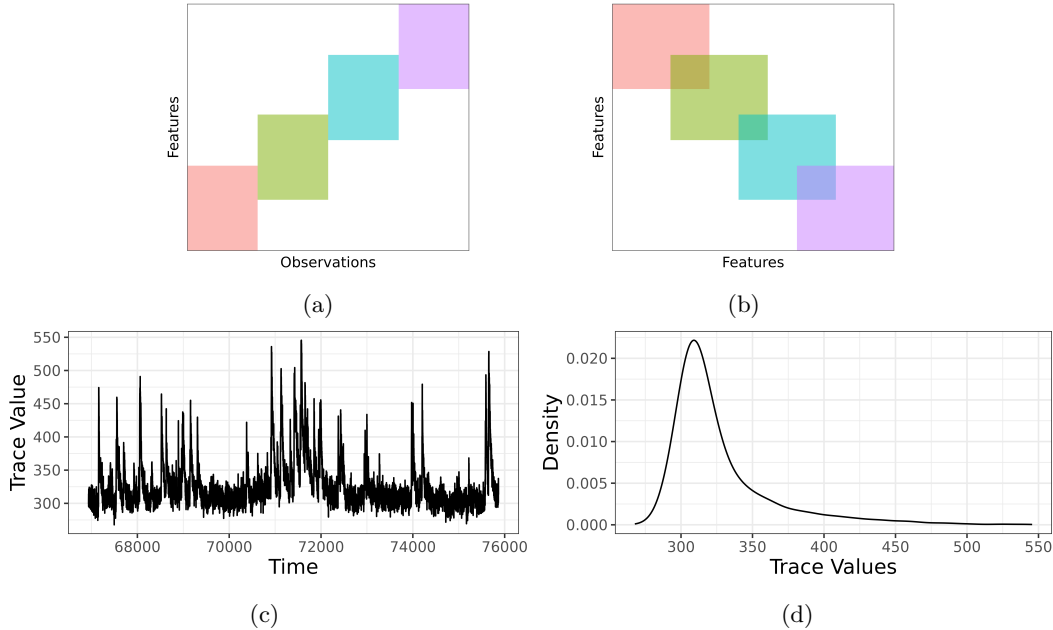


Figure 1: **(a)**: An example of a typical schema which requires Graph Quilting. Here, we have four subsets of features in a full feature set, observed across different sessions; each rectangle represents the features and observations in a particular block. **(b)**: The corresponding incomplete empirical covariance matrix for the same four patches of nodes from (a). The parts of the covariance matrix not covered by any block are never jointly observed; graph edges in this part of the covariance must be inferred from existing entries. **(c)**: Example of raw fluorescence trace for one neuron recorded in a calcium imaging experiment, showing neuronal activity over time. **(d)**: Resulting empirical density of distribution of trace values.

the nonparanormal graphical model (Liu et al., 2009; Dobra and Lenkoski, 2011). This model assumes a Gaussian copula for the joint distribution of all features while allowing arbitrary marginal distributions for each feature. Although some prior methods (Liu et al., 2009) estimate a univariate transform for each feature before graph estimation (Zhao et al., 2012), it has also been shown that nonparanormal graphical models can be estimated by applying the graphical Lasso (Yuan and Lin, 2007) on a transformed rank-based correlation matrix (Liu et al., 2012; Harris and Drton, 2013; He et al., 2017; Xue and Zou, 2012); thus, this particular procedure could be utilized in the Graph Quilting setting.

In this paper, we study two potential Graph Quilting techniques for nonparanormal graphical models for graph estimation with non-Gaussian data under block-missingness in the pairwise observation set. Our methods utilize the MAD_{GQ} and LRGQ approaches of (Vinci et al., 2019) and (Chang et al., 2022), as applied to rank-based correlation matrices; we call the nonparanormal adaptations $\text{MAD}_{\text{GQ-NPN}}$ and LRGQ-NPN , respectively. While these previous works have studied the nonparanormal graphical model using rank-based correlation matrices, such as those mentioned above, ours is the first to consider the performance of these methods in the presence of block-missingness in the empirical covariance matrix. In particular, because the missingness pattern is highly structured rather than random and the number of observed entries is relatively sparse, the performance of nonparanormal Graph Quilting will not follow directly from prior results on nonparanormal graphical models. Therefore, we explore below the nonparanormal Graph Quilting approaches both from a theoretical and empirical perspective in order to ascertain whether they are appropriate for the Graph Quilting setting.

The rest of this paper is structured as follows. In Section 2, we describe the $\text{MAD}_{\text{GQ-NPN}}$ and LRGQ-NPN procedures for nonparanormal Graph Quilting. We then show in Section 3 the conditions under which the $\text{MAD}_{\text{GQ-NPN}}$ achieves exact graph recovery for observed node pairs and minimal superset recovery for unobserved node pairs. In Section 4, we present simulation studies which compare the performances of the $\text{MAD}_{\text{GQ-NPN}}$ procedure and one of the LRGQ-NPN algorithms on data from non-Gaussian parametric dis-

tributions. Lastly, in Section 5, we investigate the efficacy of the nonparanormal Graph Quilting methods for estimating functional neuronal connectivity networks on real-world calcium imaging data sets in comparison to each other as well as to the Graph Quilting methods with Gaussian assumptions.

2 Nonparanormal Graph Quilting

2.1 Problem Set-up

We consider the nonparanormal graphical model (Liu et al., 2009), where each sample vector $X_i \in \mathbb{R}^p$ follows a nonparanormal distribution $\text{NPN}_p(f, \Sigma)$, formally defined in Definition 1.

Definition 1. Let $f = (f_1, \dots, f_p)$ be an ordered list of monotone univariate functions and let $\Sigma \in \mathbb{R}^{p \times p}$ be a positive-definite correlation matrix. Then a random vector $X = (X_1, \dots, X_p)^\top$ follows the nonparanormal distribution $\text{NPN}_p(f, \Sigma)$ if $(f_1(X_1), \dots, f_p(X_p))^\top \sim \mathcal{N}(0, \Sigma)$.

Define the precision matrix of the latent Gaussian vector $(f_1(X_1), \dots, f_p(X_p))$ as $\Theta = \Sigma^{-1}$; from this, we consider the following the graph structure that encodes the conditional dependence relationship among X : $\mathcal{G} = (V, E)$, $V = [p], E = \{(j, k) : j, k \in [p], \Theta_{j,k} \neq 0\}$. The primary interest is to recover the unknown graph structure, or equivalently, the non-zero patterns in the off-diagonal elements of Θ . When one observes i.i.d. samples X_1, \dots, X_n from this nonparanormal model, rank-based methods (Liu et al., 2012; Harris and Drton, 2013) have been proposed to learn the graph structure with selection consistency guarantees.

In the Graph Quilting setting, however, we do not have access to all features for each sample. Instead, we observe K partially overlapping blocks V_1, \dots, V_K , each of size $p_k = |V_k| < p$. The corresponding observed data matrix is denoted by $X^{(k)} \in \mathbb{R}^{n_k \times p_k}$ where n_k is the sample size for block k , and our goal is to learn the graph structure of all p features from $\{X^{(k)}\}_{k=1}^K$. We define the jointly observed feature pairs as $O = \{(i, j) : \exists 1 \leq k \leq K, i, j \in V_k\} \subset [p] \times [p]$, and let $O^c = [p] \times [p] \setminus O$ denote the feature pairs that has no joint measurement. Thus, we need to infer the graph structure of the missing portion O^c of the corresponding covariance matrix from the known pairwise observations in O .

2.2 Nonparanormal Graph Quilting Methods

In this section, we extend two prior graph quilting approaches, the MAD_{GQ} (MAXimum Determinant graph-quilting) approach (Vinci et al., 2019) and the LRGQ (Low-rank Graph Quilting) approach (Chang et al., 2022), from the Gaussian graphical model setting to the nonparanormal setting. We first note that both approaches take an estimate of the covariance/correlation $\Sigma_{i,j}$ of the Gaussian variable pairs (i, j) in $O \subset [p] \times [p]$ as the input. In the nonparanormal setting, however, we need the covariance of the latent Gaussian variables $f_1(X_1), \dots, f_p(X_p)$, which can be estimated using rank-based correlations. For our work, we consider two rank-based correlations: Spearman's rho and Kendall's tau. For each block $1 \leq k \leq K$, let $r_{i,j}^{(k)}$ be the rank of $X_{i,j}^{(k)}$ among $X_{1,j}^{(k)}, \dots, X_{n_k,j}^{(k)}$. Also, let $\bar{r}_j^{(k)} = \frac{1}{n_k} \sum_{i=1}^{n_k} r_{i,j}^{(k)} = \frac{n_k+1}{2}$. From these, we compute Spearman's rho $\hat{\rho}^{(k)} \in \mathbb{R}^{p_k \times p_k}$ and Kendall's tau $\hat{\tau}^{(k)} \in \mathbb{R}^{p_k \times p_k}$ correlations as follows:

$$\begin{aligned} \hat{\rho}_{j,l}^{(k)} &= \frac{\sum_{i=1}^{n_k} (r_{i,j}^{(k)} - \bar{r}_j^{(k)})(r_{i,l}^{(k)} - \bar{r}_l^{(k)})}{\sqrt{\sum_{i=1}^{n_k} (r_{i,j}^{(k)} - \bar{r}_j^{(k)})^2 \sum_{i=1}^{n_k} (r_{i,l}^{(k)} - \bar{r}_l^{(k)})^2}}, \\ \hat{\tau}_{j,l}^{(k)} &= \frac{2}{n_k(n_k - 1)} \sum_{1 \leq i < i' \leq n_k} \text{sign}((r_{i,j}^{(k)} - r_{i',j}^{(k)})(r_{i,l}^{(k)} - r_{i',l}^{(k)})). \end{aligned} \quad (1)$$

To obtain a $p \times p$ correlation matrix, we combine the K rank correlations $\hat{\rho}^{(k)}, \hat{\tau}^{(k)}$ together. Specifically, for any index $j \in [p]$, if $j \in V_k$, let j_k be its corresponding index in V_k . That is, $(V_k)_{j_k} = j$. Then we formally define $\hat{\rho}, \hat{\tau} \in \mathbb{R}^{p \times p}$ as follow: for $(j, l) \in O$,

$$\hat{\rho}_{j,l} = \frac{\sum_{k=1}^K \mathbb{1}_{\{j,l \in V_k\}} \hat{\rho}_{j_k,l_k}^{(k)}}{\sum_{k=1}^K \mathbb{1}_{\{j,l \in V_k\}}}, \quad \hat{\tau}_{j,l} = \frac{\sum_{k=1}^K \mathbb{1}_{\{j,l \in V_k\}} \hat{\tau}_{j_k,l_k}^{(k)}}{\sum_{k=1}^K \mathbb{1}_{\{j,l \in V_k\}}}; \quad (2)$$

otherwise, $\hat{\rho}_{j,l} = \hat{\tau}_{j,l} = 0$. As in (Liu et al., 2012), since both Spearman’s rho and Kendall’s tau rank correlations are biased for the population correlation, we apply elementwise sine function transformations to $\hat{\rho}$ and $\hat{\tau}$: for any $(j, l) \in [p] \times [p]$,

$$\widehat{\Sigma}_{j,l}^{(\rho)} = 2 \sin\left(\frac{\pi}{6} \hat{\rho}_{j,l}\right), \quad \widehat{\Sigma}_{j,l}^{(\tau)} = \sin\left(\frac{\pi}{2} \hat{\tau}_{j,l}\right). \quad (3)$$

Both initial observed correlation matrices take the value of zero in O^c , and $\widehat{\Sigma}_O^{(\rho)}, \widehat{\Sigma}_O^{(\tau)}$ serve as estimates for the population correlation Σ_O . In the following, we describe the $\text{MAD}_{\text{GQ-NPN}}$ and LRGQ-NPN approaches based on $\widehat{\Sigma}_O^{(\rho)}$ or $\widehat{\Sigma}_O^{(\tau)}$.

MAD_{GQ-NPN} approach This approach is based on a partially observed likelihood, following the MAD_{GQ} method in (Vinci et al., 2019). In a nutshell, the algorithm consists of two steps: (i) first estimating the edge set within O by minimizing an ℓ_1 -regularized log-likelihood loss under the constraint of having no edges in O^c , followed by a thresholding step that eliminates the bias effect of this artificial constraint; (ii) then using the Schur complement to estimate a superset of the edges in O^c , based on potential graph distortions in O caused by edges in O^c . The full procedure is summarized in Algorithm 1. Similar to the original MAD_{GQ} method, Algorithm 1 involves three tuning parameters: the ℓ_1 regularization parameter $\Lambda \in \mathbb{R}^{p \times p}$ in (4), and two thresholding parameters τ_1 and τ_2 for obtaining edge sets in O and O^c . For Λ , one can either simply let $\Lambda_{j,l} = \lambda$ for all $1 \leq j, l \leq p$, or choose $\Lambda_{j,l} = C_0 \sqrt{\frac{\log p}{n_{j,l}}}$ where $n_{j,l}$ is the joint sample size of node j, l together. The specific value of λ or the scaling factor C_0 can then be chosen based on the extended Bayesian information criterion (Foygel and Drton, 2010; Gao et al., 2012), which is commonly used in the graphical model literature and computationally efficient. For the first thresholding parameter τ_1 that defines the edge set $\widehat{E}_O \subset O$, we can use the stability selection approach (Liu et al., 2010) by examining the stability of \widehat{E}_O when running step 1 and 2 on randomly subsampled data. For the second thresholding parameter τ_2 , motivated by our theoretical results presented in Section 3, we can let $\tau_2 = c \sqrt{\frac{\log p}{n_k}}$ for a small constant $c > 0$. Throughout our empirical studies in this paper, we use $c = 0.05$ which turns out to work reasonably well in different settings.

Under certain assumptions on the graph structure and edge strength, (Vinci et al., 2019) shows that, in the Gaussian setting, the original MAD_{GQ} approach with sample covariance as the input is guaranteed to recover the graph structure in O and find a minimum edge superset in O^c (see Definition 2). As we will show in Section 3, such results can also be extended to our Algorithm 1 in the nonparanormal setting.

LRGQ-NPN approach Another approach we consider is extending the LRGQ method proposed by (Chang et al., 2022), which makes use of the potential low-rankness in covariance matrices. This approach is motivated by the commonly seen approximate low-rankness in many neuroscience data sets and exhibits promising performance in these applications. The LRGQ approach is a two-step procedure that first completes the covariance estimate from the partially observed sample covariance in O using appropriate low-rank matrix completion methods, then uses the completed covariance matrix as input to the graphical Lasso algorithm to produce a graph estimate. For the imputation step, (Chang et al., 2022) introduces three different imputation methods, including a block-wise SVD method (BSVDgq), a nuclear norm minimization method (NNMgq), and a non-convex gradient descent method for low-rank factorization (LRFgq). In the nonparanormal setting, we propose to apply the aforementioned two-step approach on a rank-based correlation matrix instead of the sample covariance; we summarize the full procedure in Algorithm 2. Below, throughout our empirical investigation for the LRGQ-NPN approach, we focus on the BSVDgq approach in (Chang et al., 2022) for the imputation step. More details on its implementation are included in the Appendix. Algorithm 2 also involves two tuning parameters: the rank r and the regularization parameter Λ . Similar to (Chang et al., 2022) and other prior works on low-rank matrix completion, one can choose the appropriate rank r using the Bayesian information criterion (BIC) (Burnham and Anderson, 2004). While for Λ , same as the MAD_{GQ} procedure, we can let each entry $\Lambda_{j,k}$ be the same or scale proportionally to $\sqrt{\frac{\log p}{n_{j,k}}}$. The specific values of Λ can then be chosen based on the stability criterion (Liu et al., 2010).

As has been pointed out in many prior works on graphical models (Ravikumar et al., 2011; Liu et al., 2012), the consistency of graphical Lasso hinges on sufficiently accurate covariance estimation in terms of each

Algorithm 1: MAD_{GQ}-NPN Algorithm

Input: Block indices $\{V_k\}_{k=1}^K$, Data sets $\{X^{(k)} \in \mathbb{R}^{n_k \times p_k}\}_{k=1}^K$, thresholding parameters $\tau_1, \tau_2 > 0$

1. Compute the rank-based correlation matrix $\widehat{\Sigma}_O$ as $\widehat{\Sigma}_O^{(\tau)}$ or $\widehat{\Sigma}_O^{(\rho)}$ in (3).

2. Solve the MAD_{GQlasso}-NPN problem

$$\widehat{\Theta} = \arg \max_{\Theta \succ 0, \Theta_{O^c} = 0} \log \det \Theta - \langle \widehat{\Sigma}_O, \Theta \rangle + \|\Lambda \circ \Theta\|_{1, \text{off}}. \quad (4)$$

3. Find the edge set in O : $\widehat{E}_O = \{(i, j) \in O : i \neq j, |\widehat{\Theta}_{i,j}| > \tau_1\}$

4. For $k = 1, \dots, K$, compute the Schur complement

$$\widehat{\Theta}^{(k)} = \widehat{\Theta}_{V_k, V_k} - \widehat{\Theta}_{V_k, V_k^c} \widehat{\Theta}_{V_k^c, V_k^c}^{-1} \widehat{\Theta}_{V_k^c, V_k}. \quad (5)$$

5. Find the node set

$$\widehat{W}_{\tau_1, \tau_2} = \{i \in V : \forall k \text{ s.t. } i \in V_k, \exists j \neq i, \tau_2 < |\widehat{\Theta}_{i,j}^{(k)}| < \tau_1\} \quad (6)$$

6. Obtain a superset of edges in O^c : $\widehat{E}_{O^c} = O^c \cap (\widehat{W}_{\tau_1, \tau_2} \times \widehat{W}_{\tau_1, \tau_2})$.

Output: $\widehat{E} = \widehat{E}_O \cup \widehat{E}_{O^c}$

Algorithm 2: LRGQ-NPN Algorithm

Input: Block indices $\{V_k\}_{k=1}^K$, Data sets $\{X^{(k)} \in \mathbb{R}^{n_k \times p_k}\}_{k=1}^K$, rank of full covariance matrix r .

1. Compute the rank-based correlation matrix $\widehat{\Sigma}_O$ as $\widehat{\Sigma}_O^{(\tau)}$ or $\widehat{\Sigma}_O^{(\rho)}$ in (3).

2. Obtain imputed covariance matrix $\widehat{\Sigma}^{\text{LR}}$ using low-rank covariance completion methods.

3. Apply the graphical Lasso to the imputed full covariance matrix $\widehat{\Sigma}^{\text{LR}}$ in order to obtain the estimated graph

$$\widehat{\Theta}^{\text{LR}} = \arg \min_{\Theta \succ 0} \log \det \Theta - \langle \widehat{\Sigma}^{\text{LR}}, \Theta \rangle + \|\Lambda \circ \Theta\|_{1, \text{off}}$$

Output: $\widehat{E} = \{(i, j) : i \neq j \in [p], \widehat{\Theta}_{i,j}^{\text{LR}} \neq 0\}$

entry, which implies that the two-step procedure is guaranteed to give a consistent graph selection provided that the imputation step leads to small $\|\widehat{\Sigma}^{\text{LR}} - \Sigma\|_{\infty}$. The BSVDgq method in particular has been shown in (Chang et al., 2022) to achieve sufficient imputation accuracy that eventually leads to graph selection consistency in the Gaussian setting. However, such theoretical results are based on delicate spectral analysis of sample covariance matrices, which is extremely challenging to be extended to the non-linear rank-based correlations. We leave the theoretical investigation for the LRGQ-NPN approach as future work and instead focus on empirical validation here instead.

3 Edge Recovery of MAD_{GQ}-NPN

Although the idea of using rank-based correlations to substitute the sample covariance / Pearson correlation matrix is straightforward, it is not clear if this idea would succeed in the nonparanormal graph quilting setting. In this section, we examine the theoretical properties of the MAD_{GQ}-NPN approach (Algorithm 1), giving an affirmative answer to this question by showing similar theoretical guarantees as those in (Vinci et al., 2019) established for Gaussian data. Specifically, we will show that under similar assumptions, Algorithm 1 exactly recovers the edge set in O and a minimal superset of edges in O^c . Recall the MAD_{GQlasso}-NPN

solution and its Schur complements defined in Algorithm 1, here let's first define their population versions as follows:

$$\tilde{\Theta} = \arg \max_{\Theta \succ 0, \Theta_{O^c} = 0} \log \det \Theta - \sum_{(i,j) \in O} \Theta_{i,j} \Sigma_{i,j}, \quad (7)$$

$\tilde{\Sigma} = \tilde{\Theta}^{-1}$, and for $k = 1, \dots, K$,

$$\tilde{\Theta}^{(k)} = \tilde{\Theta}_{V_k, V_k} - \tilde{\Theta}_{V_k, V_k^c} \tilde{\Theta}_{V_k^c, V_k^c}^{-1} \tilde{\Theta}_{V_k^c, V_k}. \quad (8)$$

(Vinci et al., 2019) has established nice theoretical properties for graph selection if one has access to $\tilde{\Theta}$ and $\tilde{\Theta}^{(k)}$. These results form the basis of our theory, and much of our analysis is devoted to showing the proximity of our finite sample solutions $\hat{\Theta}$ in (4) to its population counterpart $\tilde{\Theta}$, and $\hat{\Theta}^{(k)}$ in (5) to $\tilde{\Theta}^{(k)}$. In the following, we will follow the terminology and assumptions developed for the population theory in (Vinci et al., 2019).

As has been shown in (Vinci et al., 2019), hard thresholding $\tilde{\Theta}_O$ can lead to the graph recovery in O under certain assumptions on graph signals. While for the edges in O^c , the exact edge set E_{O^c} is not identifiable in the graph quilting setting. However, it is possible to recover a superset of E_{O^c} based on the distortion in the Schur complements of $\tilde{\Theta}_{V_k, V_k}$ for each block k , created by the out-of-block edges. Let the distortion created by the out-of-block edges in the block k be $\delta_{i,j}^{(k)} = \Theta_{i,j} - \tilde{\Theta}_{i,j}^{(k)}$. Given the observed covariance Σ_O and these distortion information, we define the following minimal superset of E_{O^c} as the smallest possible set that include all possible edges which cannot be ruled out without further information.

Definition 2 (Minimal Superset of E_{O^c}). *Let*

$$\mathcal{D}_{\text{off}}(\Sigma, O) = \{(i, j, k) : \delta_{i,j}^{(k)} \neq 0, i \neq j\} \quad (9)$$

be the set of known distortions over the off-diagonal elements of the Schur complements $\tilde{\Theta}^{(1)}, \dots, \tilde{\Theta}^{(K)}$, and let

$$\mathcal{A}_{\text{off}}(\Sigma, O) := \{\Sigma' \succ 0 : \Sigma'_O = \Sigma_O, \mathcal{D}_{\text{off}}(\Sigma', O) = \mathcal{D}_{\text{off}}(\Sigma, O)\} \quad (10)$$

be the set of all positive definite covariance matrices that agree with the observed Σ_O and distortions $\mathcal{D}_{\text{off}}(\Sigma, O)$. A set $\mathcal{S}_{\text{off}} \subseteq O^c$ is the minimal superset of E_{O^c} with respect to Σ_O and $\mathcal{D}_{\text{off}}(\Sigma, O)$ if it satisfies the following properties:

1. $\forall \Sigma' \in \mathcal{A}(\Sigma, O, Q)$ we have $E'_{O^c} \subseteq \mathcal{S}_{\text{off}}$;
2. $\forall \mathcal{S}' \subsetneq \mathcal{S}_{\text{off}}, \exists \Sigma' \in \mathcal{A}_{\text{off}}(\Sigma, O)$ such that $E'_{O^c} \cap (\mathcal{S}_{\text{off}} \setminus \mathcal{S}') \neq \emptyset$.

We also define the following quantities that will be useful in our theory. Let $\nu := \min_{(i,j) \in E_O} |\Theta_{i,j}|$ be the minimum signal in E_O , $\delta := \max_{(i,j) \in O, i \neq j} |\Theta_{i,j} - \tilde{\Theta}_{i,j}|$ be the maximum distortion induced by constraining $\tilde{\Theta}_{O^c} = 0$. Also let $\psi := \min_{(i,j,k): 0 < |\tilde{\Theta}_{i,j}^{(k)}| < \delta} \min\{|\tilde{\Theta}_{i,j}^{(k)}|, \delta - |\tilde{\Theta}_{i,j}^{(k)}|\}$, $d = \max_i \|\Theta_{i,\cdot}\|_0$, $\tilde{d} = \max_i \|\tilde{\Theta}_{i,\cdot}\|_0$, $\tilde{s} = \|\tilde{\Theta}\|_{0,\text{off}}$ be the number of non-zero off-diagonal elements of $\tilde{\Theta}$. Some other technical quantities include $\tilde{\kappa} = \frac{\lambda_{\max}(\tilde{\Theta})}{\lambda_{\min}(\tilde{\Theta})}$, $\kappa_{\tilde{\Sigma}} = \left\| \left\| \tilde{\Sigma} \right\| \right\|_{\infty} = \max_j \sum_{k=1}^p |\tilde{\Sigma}_{j,k}|$, $\kappa_{\tilde{\Gamma}} = \left\| \left\| (\tilde{\Gamma}_{S,S})^{-1} \right\| \right\|_{\infty}$, where S is the support set of $\tilde{\Theta}$. Let $H_i = \{j : (i, j) \in O^c\}$, $N_{H_i}(i) = N(i) \cap H_i$ be the neighborhood of i in H_i . We say that two nodes i and j are V -connected if there is a path in V connecting i and j . We also require the following assumptions:

Assumption 1 (Weak distortion compared to signal). *We assume that the maximum off-diagonal distortion of the MAD_{GQ} solution is smaller than half the signal strength in the original precision matrix: $\delta < \frac{\nu}{2}$.*

As has been proven in Theorem 3.1 in (Vinci et al., 2019), Assumption 1 can be satisfied as long as $\|\Theta_{O^c}\|_{\infty}$ is bounded above by a function of the edge weights within Θ_O ; this assumption is likely to hold as long as the pairwise observation set includes all edges with strong signal strength.

Assumption 2. *For every node $i \in V$ with $N_{H_i}(i) \neq \emptyset$, we have that for every k such that $i \in V_k$, there exists at least one node $j \in V_k \setminus \{i\}$ that is $(H_i \cup \{j\})$ -connected to some node in $N_{H_i}(i)$.*

Assumption 2 requires that if any node i has an edge in O^c , then for any block it belongs to, there exists a path that starts from i and an edge in O^c , and eventually back to this block. This assumption ensures that any edge (i, j) in O^c would cause certain distortions in the blocks i and j belong to. Therefore, given the distortion set $\mathcal{D}_{\text{off}}(\Sigma, O)$, it is possible to identify the node set with edges in O^c . However, we can't directly compute the distortion $\delta_{i,j}^{(k)}$, a discrepancy between the unknown $\Theta_{i,j}$ and $\tilde{\Theta}_{i,j}$. Instead, we can only assume that such discrepancy leads to a small non-zero $\tilde{\Theta}_{i,j}$. This motivates our following assumption:

Assumption 3. *If $\delta_{i,\setminus i}^{(k)} \neq 0$, then there exists $j \neq i$ such that $0 < |\tilde{\Theta}_{ij}^{(k)}| < \delta$.*

Assumption 4 (Incoherence condition). *Let $\Gamma = \tilde{\Sigma} \otimes \tilde{\Sigma}$, $S = \{(j, l) : \tilde{\Theta}_{j,l} \neq 0\}$. We assume $\max_{e \in O \cap S^c} \|\Gamma_{e,S} \Gamma_{S,S}^{-1}\|_1 \leq 1 - \alpha$ for some $0 < \alpha \leq 1$.*

Similar incoherence conditions are commonly assumed in the literature of graphical models (Ravikumar et al., 2011).

Assumption 5 (Sufficient block measurements). *The K blocks cover all nodes: $\cup_{k=1}^K V_k = [p]$, and at least one off-diagonal element: $|O| > p$.*

This is a mild assumption on the block measurements, which is typically satisfied by our motivating neuroscience applications.

Assumption 6 (Regularization parameter). $\Lambda_{j,l} = \frac{C_0}{\alpha} \sqrt{\frac{\log p}{\min_k n_k}}$ for all $(j, l) \in O$ and some universal constant $C_0 > 0$.

Assumptions 1-6 also appear in (Vinci et al., 2019) in the Gaussian graphical model setting. Note that we do not require any additional assumptions when extending the theoretical guarantees to the nonparanormal setting, while accommodating for strictly weaker assumptions on the joint distribution.

Theorem 1. *Suppose that Assumptions 1-6 hold, and there exist at least one edge in the graph encoded by Θ and $\tilde{\Theta}$: $d, \tilde{d} > 2$. Then we have the following guarantees for Algorithm 1 with probability at least $1 - \sum_k p_k^{-10}$:*

- **Exact recovery in O .** *If*

$$n_k > \left[\frac{C_0}{4} \kappa_{\tilde{\Gamma}} \left(1 + \frac{8}{\alpha} \right) \left(\left(\frac{\nu}{2} - \delta \right)^{-1} + 3 \left(1 + \frac{8}{\alpha} \right) (\kappa_{\tilde{\Sigma}} + \kappa_{\tilde{\Sigma}}^3 \kappa_{\tilde{\Gamma}} \tilde{d}) \right) \right]^2 \log p_k, \quad (11)$$

$$\delta + \varepsilon_1 \leq \tau_1 < \nu - \delta - \varepsilon_1, \text{ where } \varepsilon_1 = \frac{C_0}{4} \kappa_{\tilde{\Gamma}} \left(1 + \frac{8}{\alpha} \right) \max_k \sqrt{\frac{\log p_k}{n_k}}, \text{ then } \hat{E}_O = E_O.$$

- **Minimal superset recovery in O^c .** *If*

$$n_k > C_0 \kappa_{\tilde{\Gamma}}^2 \left(1 + \frac{8}{\alpha} \right)^2 \left[\frac{9\tilde{\kappa}^4}{4\psi^2} + \frac{1}{4\lambda_{\min}(\tilde{\Theta})^2} \right] \min\{p + \tilde{s}, \tilde{d}^2\} \log p_k, \quad (12)$$

$$\varepsilon_2 \leq \tau_2 < \psi - \varepsilon_2, \delta - \varepsilon_2 < \tau_1 \leq \nu - \varepsilon_2, \text{ where } \varepsilon_2 = \frac{3C_0}{4} \kappa_{\tilde{\Gamma}} \left(1 + \frac{8}{\alpha} \right) \tilde{\kappa}^2 \min\{\sqrt{p + \tilde{s}}, \tilde{d}\} \max_k \sqrt{\frac{\log p_k}{n_k}}, \text{ then } \hat{E}_{O^c} = \mathcal{S}_{\text{off}}.$$

The proof of Theorem 1 can be found in the Appendix. Theorem 1 suggests that under the same population assumptions as the Gaussian graph quilting setting in (Vinci et al., 2019), as long as the sample size for each block is sufficiently large: $n_k = \Omega(\tilde{d}^2 \log p_k)$, and the thresholding parameters are appropriately chosen: $\tau_1 \in [\delta + C \max_k \sqrt{\frac{\log p_k}{n_k}}, \nu - \delta - C \max_k \sqrt{\frac{\log p_k}{n_k}})$, $\tau_2 \asymp \tilde{d} \max_k \sqrt{\frac{\log p_k}{n_k}}$, we can achieve exact recovery for edges in O and construct a minimal superset for edges in O^c . This result is comparable to the main theory in (Vinci et al., 2019) for Gaussian graphical model, although we are considering a strictly broader distribution family. To prove Theorem 1, we first extend the existing error bounds for rank-based correlation matrices (Liu et al., 2012) in the full data setting to our modified correlation estimates defined in 2.2, which is computed from K semi-overlapping blocks of measurements. We then utilize this error bound to show the proximity of $\hat{\Theta}$ and its Schur complements $\hat{\Theta}^{(k)}$ to their population counterparts, which eventually leads to Theorem 1 when combined with the population theory developed in (Vinci et al., 2019).

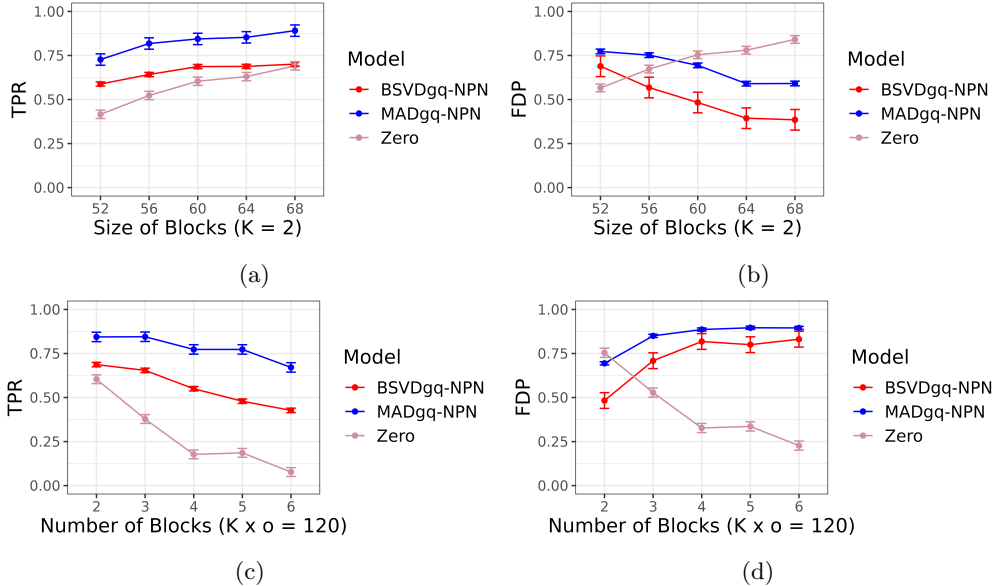


Figure 2: Performance of MAD_{GQ} -NPN, $BSVD_{gq}$ -NPN, and zero imputation on simulated data from a Gamma distribution. (a) TPR, changing block size. (b) FDP, changing block size. (c) TPR, number of blocks. (d) FDP, changing number of blocks.

4 Simulation Studies

We now investigate the empirical performance of the nonparanormal Graph Quilting procedures outlined in Section 2 on simulated data. For each of the simulation trials, we create synthetic block observation patterns by randomly ordering the features and assigning them to K partially overlapping blocks of size o . Data is generated for each block from multivariate Gaussian data from a sparse inverse covariance matrix with a small-world structure and then perform copula transform on each column to a non-Gaussian distribution. Rank-based correlations are calculated entry-wise for each pair of features in the observation set, with correlations averaged for pairs observed in multiple blocks. Our goal is to recover the nonzero entries in the population sparse inverse covariance matrix of the unobserved Gaussian variable. Below, we compare the MAD_{GQ} -NPN approach and one of the LRGQ-NPN procedures, namely the block SVD ($BSVD_{gq}$ -NPN) approach, along with a basic zero imputation procedure in which the missing entries of the correlation matrix are imputed as 0 before applying the graphical Lasso algorithm. The methods are evaluated using the true positive rate (TPR) and false discovery proportion (FDP) of their respective resulting graph estimates as compared to the true underlying graph; in particular, we run 50 replications on each set of simulation parameters, with new random block assignment in each replication, and show the average and standard deviation of the TPR and FDP of edge selection for each method. Hyperparameter selection is performed via optimal F-1 score tuning with respect to the true graph.

We first test the nonparanormal Graph Quilting methods with Spearman correlation matrices calculated on data containing 100 features generated from a Gamma distribution with shape parameter 5 and scale parameter 1. For each block, 2000 observations are generated per feature. Figures 2a and 2b show the TPR and FDP of each method compared to the true underlying graph when the size of the block o is 52, 56, 60, 64, and 68 while the number of blocks is held constant at 2, and Figures 2c and 2d show the TPR and FDP for $K = 2, 3, 4, 5$ and 6 blocks while keeping the total number of observed node pairs across all blocks ($K \times o$) constant at 120. From these results, we see that both methods achieve a consistently high true positive rate for edge recovery, and generally outperforms the zero imputation method. Notably, even though the low-rank assumption inherent to the $BSVD_{gq}$ -NPN method is not met here, the method is still able to recover the true edges of the graph at a decently high rate. Comparing the two nonparanormal Graph Quilting methods, we see that the MAD_{GQ} -NPN approach consistently has a higher TPR and FDP compared to $BSVD_{gq}$ -NPN;

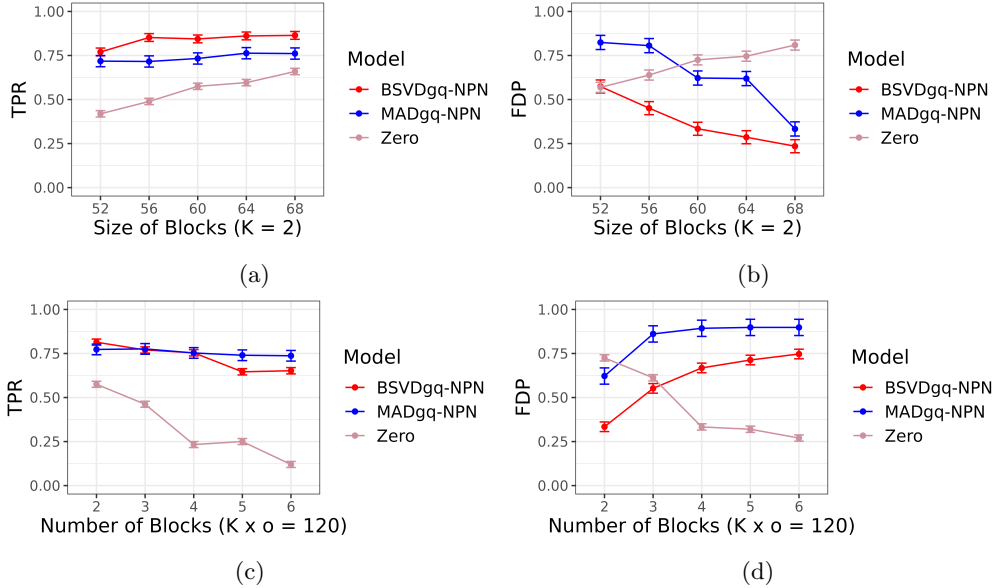


Figure 3: Performance of MAD_{GQ} -NPN, BSVDgq-NPN, and zero imputation on simulated data from a Cauchy distribution with low-rank covariance. (a) TPR, changing block size. (b) FDP, changing block size. (c) TPR, changing number of blocks. (d) FDP, changing number of blocks.

this result follows what we expect, as the former approach is designed to construct a superset of the true edges for the unobserved entries in the covariance matrix and thus will return an estimate with both more true positives and false positives compared to BSVDgq-NPN. Across different simulation parameters, we generally observe that TPR is higher and FDP is lower for the estimates from both methods when there are fewer blocks and when each block is larger, which we would expect to see as these conditions effectively provide more samples for estimation. Additionally, the difference in performance between the two nonparanormal Graph Quilting methods appear to be fairly consistent across the different block sizes and number of blocks.

We also evaluate the nonparanormal Graph Quilting methods on data simulated from a Cauchy distribution with mean 0 and scale parameter 3 with 2000 observations and 100 features, from which a Kendall correlation matrix is calculated and used as the input to the graphical Lasso. For this particular experiment, we consider the case where the underlying covariance matrix is approximately low-rank; this is generated via the spiked covariance model (Johnstone, 2001), and we also enforce a small-world graph structure in its inverse. Figures 3a and 3b compare the MAD_{GQ} -NPN and BSVDgq-NPN methods in terms of TPR and FDR for edge selection for $K = 2$ blocks and varying block size o is 52, 56, 60, 64, and 68, and Figures 3c and 3d compare the same methods for $K = 2, 3, 4, 5$ and 6 blocks with a constant total number of observations ($K \times o$) of 120. Both nonparanormal Graph Quilting methods perform well in terms of true positive rate for edge recovery here as well, and both considerably outperform the zero imputation approach. As opposed to the previous simulation study in which the MAD_{GQ} -NPN method outperformed the BSVDgq-NPN method in terms of selecting true edges in the graph, we see in this case that the latter outperforms the former for both the TPR and FDP metrics. The relative performance of the two nonparanormal Graph Quilting methods matches what we would expect from this particular simulation setting, as the structure of the full true underlying covariance matrix more closely match the model set-up of the BSVDgq-NPN method, and also aligns with comparative results seen from (Chang et al., 2022) comparing Graph Quilting methods under a Gaussian assumption. Even in this case, though, the MAD_{GQ} -NPN method still recovers the true edges of the underlying graph reasonably well. These results show that the choice of which of the nonparanormal Graph Quilting approach to apply for a problem will depend whether a low-rank assumption makes sense in the particular scientific context. Additionally, as above, we observe that performance generally improves with larger blocks and with a fewer total number of blocks.

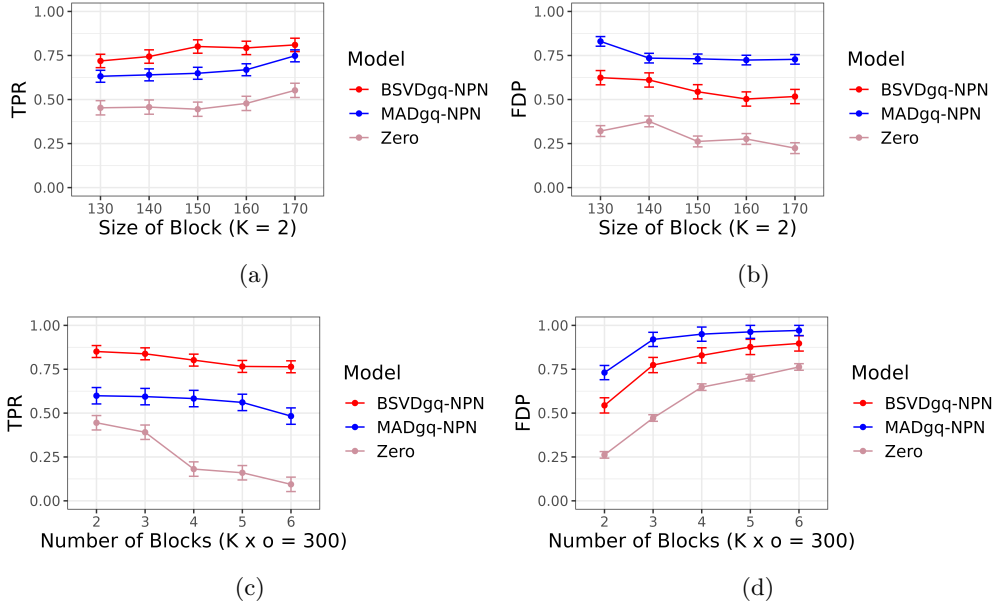


Figure 4: Performance of MAD_{GQ} -NPN, BSVDgq-NPN, and zero imputation on Allen Institute data. (a) TPR, changing block size. (b) FDP, changing block size. (c) TPR, changing number of blocks. (d) FDP, changing number of blocks.

5 Calcium Imaging Example

We now study the nonparanormal Graph Quilting procedures on a real-world calcium imaging data set in order to assess the applicability of these methods for estimating functional neuronal connectivity. The data come from the Allen Institute (de Vries et al., 2016) and contains functional activity recordings for 227 neurons in a mouse V1 cortex during spontaneous activity across approximately 9000 time points. For this analysis, we compare the performances of the MAD_{GQ} -NPN and BSVDgq-NPN nonparanormal Graph Quilting methods to each other, as well as to a zero imputation approach, in a similar fashion to the methodology in Section 4. We also compare the two nonparanormal Graph Quilting methods to their analogous Gaussian-based procedures.

To do the former, we measure the performances of the MAD_{GQ} -NPN, BSVDgq-NPN, and zero imputation procedure by how well the graph estimates from each nonparanormal Graph Quilting method on rank-based correlation matrices with synthetic block-missingness recovers the edge structure of the graph estimated using the nonparanormal graphical model on the same rank-based correlation matrix with all pairwise entries observed. Specifically, we calculate the Spearman correlation matrix for all observed neurons using binned spike counts and apply the graphical Lasso to the fully observed covariance, the result of which we consider as the true underlying graph structure. We create artificial block-missingness in the empirical covariance matrix by randomly assigning features to K partially overlapping blocks of size o and masking all pairwise entries in the covariance which are not contained in any block. The masked Spearman correlation matrix is then used as input for the nonparanormal Graph Quilting methods. We show the average and standard deviation of the TPR and FDR for recovering the graph estimate on the full Spearman covariance matrix for each method across 50 replications on each set of parameters, with new random block assignments each replication. Hyperparameter selection is performed using optimal F-1 score with respect to the graph estimated from the graphical Lasso fit on the fully observed data with the rank-based correlation matrix.

Figures 4a and 4b show the TPR and FDP of each method compared to the true underlying graph when the size of the block o is 130, 140, 150, 160, and 170 while the number of blocks is held constant at 2, and Figures 4c and 4d show the TPR and FDP for $K = 2, 3, 4, 5$ and 6 blocks while keeping the total number of observations across all blocks ($K \times o$) constant at 300. In general, both nonparanormal Graph Quilting methods are able to recover most of edges as the graph estimated with the nonparanormal graphical

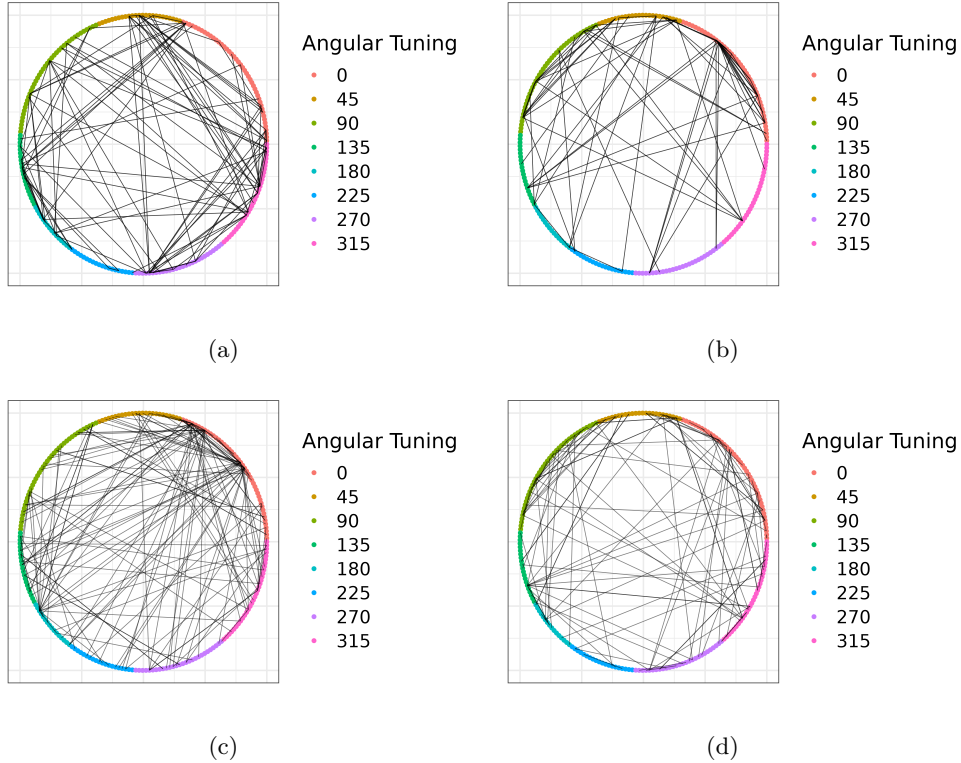


Figure 5: Estimated functional connectivity networks from Graph Quilting methods on Allen Institute data. Nodes are colored by visual angular tuning category. (a) BSVDgq. (b) BSVDgq-NPN. (c) MAD_{GQ}. (d) MAD_{GQ}-NPN.

model when all features are observed simultaneously, which shows that both methods can reliably recover the edges in functional neuronal connectivity networks derived from calcium imaging data that would be present if all neurons were observed simultaneously. However, we also observe a relatively high FDP for both methods, which seems to show that both methods tend to slightly overselect the total number of edges in the underlying full graph. The BSVDgq-NPN method outperforms MAD_{GQ}-NPN for edge recovery in terms of both TPR and FDP; this can likely be attributed to the approximate low-rank structure often found in the empirical covariance matrices from calcium imaging data (Stringer et al., 2019). Also, as seen in Section 4, all methods perform better with fewer blocks and with larger block sizes.

We then compare the functional neuronal connectivity graphs from the nonparanormal Graph Quilting methods to those found using Graph Quilting with a Gaussian assumption. Specifically, we use the MAD_{GQ} and BSVDgq Graph Quilting methods to obtain graph estimates on the same data set with the same artificial block-missingness pattern as above, and compare the selected edges to functional connectivity graphs estimated by MAD_{GQ}-NPN and BSVDgq-NPN using neural properties from provided metadata. We first assess each of the estimated functional connectivity networks by the proportion of edges that connect pairs of neurons with the same visual angular tuning category. In the neuroscience literature, it has been hypothesized that neurons are tuned such that they fire in the presence of specific stimuli (Sakia and Miyashita, 1994) and that neurons with the similar tunings are more likely to be functionally connected (Stevenson et al., 2012). Thus, we expect a sizable proportion of the edges in the estimated functional connectivity networks to link pairs of neurons within the same tuning category. For this particular calcium imaging data set, neural angular tuning is categorized into 8 different bins, each comprising 45 degree intervals. Hyperparameter tuning for the BSVDgq and BSVDgq-NPN methods is performed using the extended Bayesian information criterion with respect to the original data; for the MAD_{GQ} and MAD_{GQ}-NPN methods, in order to create a fair comparison between methods, we tune the thresholding parameters such that the number of edges is

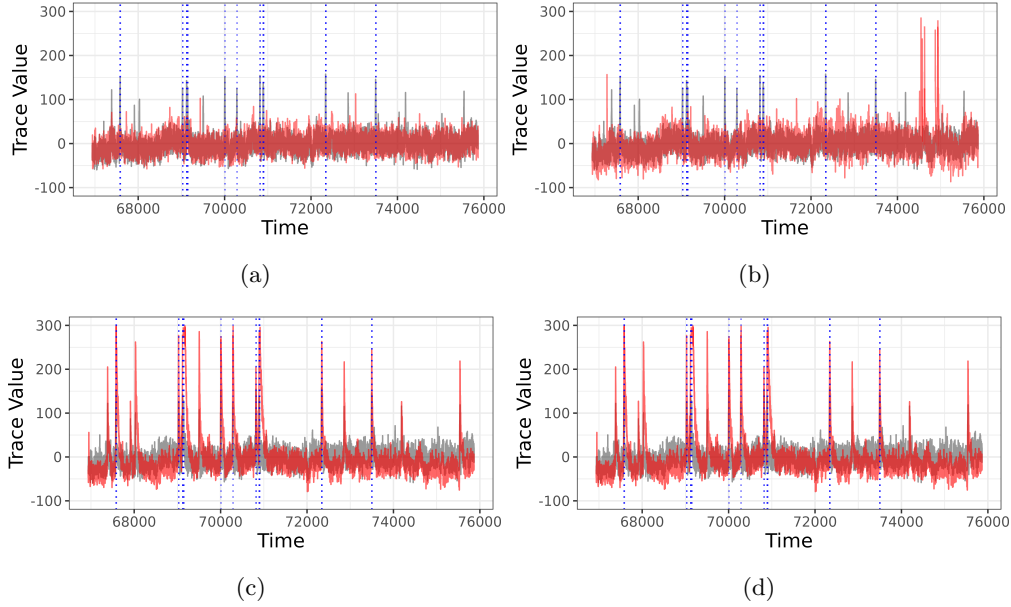


Figure 6: Fluorescence traces of one particular neuron (in grey) and edge neighbors (in red) from functional connectivity graphs estimated via BSVDgq ((a, b)) and BSVDgq-NPN ((c, d)).

approximately similar to the estimates from BSVDgq and BSVDgq-NPN.

Figures 5a and 5b show examples of estimated functional connectivity networks from the BSVDgq and BSVDgq-NPN methods, and Figures 5c and 5d show estimated functional connectivity networks from the MAD_{GQ} and MAD_{GQ} -NPN methods, respectively. Structurally, we see that the graph estimates from the nonparanormal Graph Quilting methods are much more likely to be comprised of edges between neurons with the same angular tuning category. Specifically, across different replications with synthetic block-missingness, the BSVDgq-NPN graph estimates contain an average of 38.9% of edges that link neurons with the same tuning category, compared to 21.4% of edges in the BSVDgq estimates. Similarly, we see that 46.8% of edges in the MAD_{GQ} -NPN graph estimates are between pairs of neurons in the same tuning bin, as opposed to just 28.7% in the MAD_{GQ} graph estimates.

We also compare the recorded firing activity of one particular example neuron and its selected edge neighbors in the the functional connectivity graphs estimated from the BSVDgq and BSVDgq-NPN methods in terms of how closely the neural firing patterns match one another. Specifically, for the problem of functional neuronal connectivity, our goal is to find neurons with consistent synchronous firing activity across time, which is represented by contemporaneous large positive spikes in the fluorescence traces (Smetters et al., 1996; Turaga et al., 2013). In Figures 6a and 6b, we visualize the fluorescence trace of the selected neuron, overlaid with the fluorescence traces neurons which are edge neighbors unique to the BSVDgq graph; we also do the same in Figures 6c and 6d for neurons that are edge neighbors unique to the BSVDgq-NPN graph. The top 10 periods of spiking activity of the example selected neuron are represented via blue dotted lines in the plots. From the results, we see that the firing activity of the selected neuron seems to match relatively closely with the edge neighbors selected only in the graph estimate from the BSVDgq-NPN algorithm. On the other hand, the edge neighbors selected only by the BSVDgq graph do not appear to have the same firing pattern. Quantitatively, the top 10 firing times for the selected neuron and its edge neighbors match 72.4% of the time for the BSVDgq-NPN functional connectivity graph estimates, as opposed to just 24.5% for the BSVDgq functional connectivity graphs. Overall, from this real-world calcium imaging data study, we see that nonparanormal Graph Quilting provides more logical functional connectivity estimates in the neuroscience context compared to the ordinary Graph Quilting procedures.

6 Discussion

In this work, we have presented two potential approaches to nonparanormal Graph Quilting, MAD_{GQ} -NPN and $DSVDgq$ -NPN, which broaden the scope of Graph Quilting procedures to be applicable in the nonparanormal graphical model setting. We demonstrate theoretical properties of the MAD_{GQ} -NPN method, showing criterion for exact edge recovery in the observed portion and minimum superset recovery in the missing portion of the graph. Through our empirical studies, we demonstrate that both nonparanormal Graph Quilting methods can be effective for edge selection for non-Gaussian data depending on the structure of the underlying covariance matrix. Through our real-world calcium imaging data example, we show that the nonparanormal Graph Quilting methods can be used to recover the same functional neuronal connectivity network edges from calcium imaging data in the presence of non-simultaneous observations for the full population of neurons as would be found if all neurons are observed concurrently, and that these methods can be applied to estimate more appropriate functional neuronal connectivity networks from calcium imaging data compared to Gaussian methods.

There are many potential directions for future research that can be taken from our work. While we have characterized the theoretical performance of the MAD_{GQ} -NPN approach, we do not currently have any guarantees for the $LRGQ$ -NPN methods. Methodologically, extensions to the nonparanormal Graph Quilting procedure to account for potential other data effects such as latent variables, autocorrelations, or covariates could improve graph estimation and edge selection accuracy. Also, the nonparanormal graphical models could be applied to research problems in other fields where joint observations may be missing, such as RNA-seq in genomics and signal processing in power systems. In conclusion, our work has helped to extend graph inference for nonparanormal graphical models in the presence of block-missingness in the observed covariance matrix, with theoretical guarantees for performance and promising empirical results for calcium imaging data.

Acknowledgements

The authors gratefully acknowledge support by NSF NeuroNex-1707400, NIH 1R01GM140468, and NSF DMS-2210837.

References

- Allen, G. and Liu, Z. (2013). A local poisson graphical model for inferring networks from sequencing data. *IEEE transactions on nanobioscience*, 12(3):189–198.
- Berens, P., Theis, L., Stone, J., Sofroniew, N., Tolias, A., Bethge, M., and Freeman, J. (2017). Standardizing and benchmarking data analysis for calcium imaging. *Computational and Systems Neuroscience Meeting (COSYNE 2017)*, pages 66–67.
- Burnham, K. P. and Anderson, D. R. (2004). Multimodel inference: understanding aic and bic in model selection. *Sociological methods & research*, 33(2):261–304.
- Carrillo-Reid, L., Han, S., O’Neil, D., Taralova, E., Jebara, T., and Yuste, R. (2021). Identification of pattern completion neurons in neuronal ensembles using probabilistic graphical models. *Journal of Neuroscience*, 41(41):8577–8588.
- Chang, A. and Allen, G. (2021). Subbotin graphical models for extreme value dependencies with applications to functional neuronal connectivity. *arXiv preprint arXiv:2106.11554*.
- Chang, A., Zheng, L., and Allen, G. I. (2022). Low-rank covariance completion for graph quilting with applications to functional connectivity. *arXiv preprint arXiv:2209.08273*.
- Chen, L., Wainwright, M., Cetin, M., and Willsky, A. (2016). Data association based on optimization in graphical models with application to sensor networks. *Mathematical and computer modelling*, 43(9-10):1114–1135.

- Dasarathy, G., Singh, A., Balcan, M., and Park, J. (2016). Active learning algorithms for graphical model selection. *Artificial Intelligence and Statistics*, pages 1356–1364.
- de Vries, S., Lecoq, J., Buice, M., Groblewski, P., Ocker, G., Oliver, M., Feng, D., Cain, N., Ledochowitsch, P., Millman, D., and Roll, K. (2016). Dataset: Allen institute mindscape program. *Allen Institute. Dataset.*, https://observatory.brain-map.org/visualcoding/search/cell_list?experiment_container_id=511510989&sort_field=p_sg&sort_dir=asc.
- Deco, G., McIntosh, A., Shen, K., Hutchison, R., Menon, R., Everling, S., Hagmann, P., and Jirsa, V. (2014). Identification of optimal structural connectivity using functional connectivity and neural modeling. *Journal of Neuroscience*, 34(23):7910–7916.
- Dobra, A. and Lenkoski, A. (2011). Copula Gaussian graphical models and their application to modeling functional disability data. *The Annals of Applied Statistics*, 5(2A):969 – 993.
- Feldt, S., Bonifazi, P., and Cossart, R. (2011). Dissecting functional connectivity of neuronal microcircuits: experimental and theoretical insights. *Trends in neurosciences*, 34(5):225–236.
- Finegold, M. and Drton, M. (2011). Robust graphical modeling of gene networks using classical and alternative t-distributions. *The Annals of Applied Statistics*, pages 1057–1080.
- Fingelkurts, A., Fingelkurts, A., and Kähkönen, S. (2005). Functional connectivity in the brain—is it an elusive concept? *Neuroscience & Biobehavioral Reviews*, 28(8):827–836.
- Foygel, R. and Drton, M. (2010). Extended bayesian information criteria for gaussian graphical models. *Advances in neural information processing systems*, 23.
- Gao, X., Pu, D. Q., Wu, Y., and Xu, H. (2012). Tuning parameter selection for penalized likelihood estimation of gaussian graphical model. *Statistica Sinica*, pages 1123–1146.
- Garofalo, M., Nieuws, T., Massobrio, P., and Martinoia, S. (2009). Evaluation of the performance of information theory-based methods and cross-correlation to estimate the functional connectivity in cortical networks. *PloS one*, 4(8):e6482.
- Grienberger, C. and Konnerth, A. (2012). Imaging calcium in neurons. *Neuron*, 73(5):862–885.
- Harris, N. and Drton, M. (2013). Pc algorithm for nonparanormal graphical models. *Journal of Machine Learning Research*, 14(11):3365–3383.
- Hartemink, A., Gifford, D., Jaakkola, T., and Young, R. (2000). Using graphical models and genomic expression data to statistically validate models of genetic regulatory networks. *Biocomputing*, pages 422–433.
- He, Y., Zhang, X., Wang, P., and Zhang, L. (2017). High dimensional gaussian copula graphical model with fdr control. *Computational Statistics & Data Analysis*, 113:457–474.
- Horwitz, B. (2003). The elusive concept of brain connectivity. *Neuroimage*, 19(2):466–470.
- Johnstone, I. (2001). On the distribution of the largest eigenvalue in principal components analysis. *The Annals of statistics*, 29(2):295–327.
- Liu, H., Han, F., Yuan, M., Lafferty, J., and Wasserman, L. (2012). High-dimensional semiparametric gaussian copula graphical models. *The Annals of Statistics*, 40(4):2293–2326.
- Liu, H., Lafferty, J., and Wasserman, L. (2009). The nonparanormal: Semiparametric estimation of high dimensional undirected graphs. *Journal of Machine Learning Research*, 10(10):2295–2328.
- Liu, H., Roeder, K., and Wasserman, L. (2010). Stability approach to regularization selection (stars) for high dimensional graphical models. *Advances in neural information processing systems*, 23.

- Massa, M. S. and Chiogna, M. (2013). Effectiveness of combinations of gaussian graphical models for model building. *Journal of Statistical Computation and Simulation*, 83(9):1602–1612.
- Masud, M. and Borisyuk, R. (2011). Statistical technique for analysing functional connectivity of multiple spike trains. *Journal of Neuroscience Methods*, 196(1):201–219.
- Pillow, J., Shlens, J., Paninski, L., Sher, A., Litke, A., Chichilnisky, E., and Simoncelli, E. (2008). Spatio-temporal correlations and visual signalling in a complete neuronal population.]. *Nature*, 454(7207):995–999.
- Pnevmatikakis, E., Soudry, D., Gao, Y., Machado, T., Merel, J., Pfau, D., Reardon, T., Mu, Y., Lacefield, C., Yang, W., and Ahrens, M. (2016). Simultaneous denoising, deconvolution, and demixing of calcium imaging data. *Neuron*, 89(2):285–299.
- Ravikumar, P., Wainwright, M. J., Raskutti, G., and Yu, B. (2011). High-dimensional covariance estimation by minimizing ℓ_1 -penalized log-determinant divergence. *Electronic Journal of Statistics*, 5:935–980.
- Sakia, K. and Miyashita, Y. (1994). Neuronal tuning to learned complex forms in vision. *Neuroreport*, 5:829–832.
- Smetters, D., Majewska, A., and Yuste, R. (1996). Detecting action potentials in neuronal populations with calcium imaging. *Methods*, 18(2):215–221.
- Stetter, O., Battaglia, D., Soriano, J., and Geisel, T. (2012). Model-free reconstruction of excitatory neuronal connectivity from calcium imaging signals. *PLoS Computational Biology*, 8:e1002653.
- Stevenson, I., London, B., Oby, E., Sachs, N., Reimer, J., Englitz, B., David, S., Shamma, S., Blanche, T., Mizuseki, K., and Zandvakili, A. (2012). Neuronal tuning to learned complex forms in vision. *Neuroreport*, 8(11):e1002775.
- Stevenson, I., Rebesco, J., Miller, L., and Körding, K. (2008). Inferring functional connections between neurons. *Current opinion in neurobiology*, 18(6):582–588.
- Stringer, C., Pachitariu, M., Steinmetz, N., Reddy, C., Carandini, M., and Harris, K. (2019). Spontaneous behaviors drive multidimensional, brainwide activity. *Science*, 364(6437):eaav789.
- Subramaniyan, M., Ecker, A., Patel, S., Cotton, R., Bethge, M., Pitkow, X., Berens, P., and Tolias, A. (2018). Faster processing of moving compared with flashed bars in awake macaque v1 provides a neural correlate of the flash lag illusion. *Journal of Neurophysiology*, 120(5):2430–2452.
- Turaga, S., Buesing, L., Packer, A., Dalglish, H., Pettit, N., Hausser, M., and Macke, J. (2013). Inferring neural population dynamics from multiple partial recordings of the same neural circuit. *Advances in Neural Information Processing Systems*, 26.
- Vinci, G., Dasarathy, G., and Allen, G. I. (2019). Graph quilting: graphical model selection from partially observed covariances. *arXiv preprint arXiv:1912.05573*.
- Vinci, G., Ventura, V., Smith, M., and Kass, R. (2018). Adjusted regularization in latent graphical models: Application to multiple-neuron spike count data. *The annals of applied statistics*, 12(2):1068–1095.
- Vogel, D. and Fried, R. (2011). Elliptical graphical modelling. *Biometrika*, 98(4):935–951.
- Xue, L. and Zou, H. (2012). Regularized rank-based estimation of high-dimensional nonparanormal graphical models. *The Annals of Statistics*, 40(5):2541–2571.
- Xue, W., Kang, J., Bowman, F., Wager, T., and Guo, J. (2014). Identifying functional co-activation patterns in neuroimaging studies via poisson graphical models. *Biometrics*, 70(4):812–822.
- Yang, E., Ravikumar, P., Allen, G. I., and Liu, Z. (2015). Graphical models via univariate exponential family distributions. *The Journal of Machine Learning Research*, 16(1):3813–3847.

- Yang, E., Ravikumar, P. K., Allen, G. I., and Liu, Z. (2013). On poisson graphical models. *Advances in neural information processing systems*, 26.
- Yang, Z., Ning, Y., and Liu, H. (2018). On semiparametric exponential family graphical models. *The Journal of Machine Learning Research*, 19(1):2314–2372.
- Yatsenko, D., Josić, K., Ecker, A., Froudarakis, E., Cotton, R., and Tolias, A. (2015). Improved estimation and interpretation of correlations in neural circuits. *PLoS computational biology*, 11(3):e1004083.
- Yuan, M. and Lin, Y. (2007). Model selection and estimation in the gaussian graphical model. *Biometrika*, 94(1):19–35.
- Zhao, T., Liu, H., Roeder, K., Lafferty, J., and Wasserman, L. (2012). The huge package for high-dimensional undirected graph estimation in r. *Journal of Machine Learning Research*, 14(11):3365–3383.

A Algorithmic Details

In our LRGQ-NPN approach, one key step is to impute the covariance matrix $\widehat{\Sigma}^{\text{LR}}$ from partially computed $\widehat{\Sigma}_O = \widehat{\Sigma}_O^{(\tau)}$ or $\widehat{\Sigma}_O^{(\rho)}$. We consider the following BSVDgq algorithm (Algorithm 3) proposed in (Chang et al., 2022) for this step.

Algorithm 3: Spiked Block Singular Value Decomposition (Spiked BSVD_{gq}) (Chang et al., 2022)

Input: $\{V_k, k \in 1, \dots, K\}$, $\widehat{\Sigma}_O \in \mathbb{R}^{p \times p}$, $r > 0$.

Initialize: $\widehat{H} = \mathbf{0}_{p \times r}$, $A = V_1$, $\widehat{q} = \text{median}(\{\widehat{\Sigma}_{ii}, 1 \leq i \leq p\})$.

Find low-rank solution for first patch:

1. Calculate SVD of $(\widehat{\Sigma} - \widehat{q}\mathbf{I})_{V_1, V_1} = \mathbf{W}\mathbf{\Lambda}\mathbf{U}^T$.
2. Set \mathbf{h} as indices of the largest r diagonal elements of $\mathbf{\Lambda}$.
3. Set $\mathbf{C}_{V_1, :} = \mathbf{U}_{:, \mathbf{h}}\mathbf{\Lambda}_{\mathbf{h}, \mathbf{h}}^{1/2}$.

For $s \in 2, \dots, K$

1. Find low-rank solution for s -th patch:
 - (a) Calculate SVD of $(\widehat{\Sigma} - \widehat{q}\mathbf{I})_{V_s, V_s} = \mathbf{W}\mathbf{\Lambda}\mathbf{U}^T$.
 - (b) Set \mathbf{h} as indices of the largest r diagonal elements of $\mathbf{\Lambda}$.
 - (c) Calculate $\mathbf{D} = \mathbf{U}_{:, \mathbf{h}}\mathbf{\Lambda}_{\mathbf{h}, \mathbf{h}}^{1/2}$.
2. Merge with previous patches:
 - (a) Find overlaps $E = \{A : a \in V_s\}$, $J = \{j : V_s[j] \in A\}$.
 - (b) Calculate SVD of $(\mathbf{D}_J^T \mathbf{C}_{E, :}) = \mathbf{W}\mathbf{\Lambda}\mathbf{U}^T$.
 - (c) Set $\mathbf{M} = \mathbf{C}_{E, :}$, $\mathbf{C}_{V_s, :} = \mathbf{D}\mathbf{W}\mathbf{U}^T$.
3. Update $\mathbf{C}_E \leftarrow \bigcup_{k=1}^s \mathbf{M}_s$

return $\widehat{\Sigma} = \mathbf{C}\mathbf{C}^\top$.

B Proofs

For completeness, here we restate our MAD_{GQ}-NPN algorithm, its theory and assumptions presented in the main paper. The rank-based correlation is defined as follows:

$$\widehat{\Sigma}_{j,l}^{(\rho)} = 2 \sin\left(\frac{\pi}{6} \widehat{\rho}_{j,l}\right), \quad \widehat{\Sigma}_{j,l}^{(\tau)} = \sin\left(\frac{\pi}{2} \widehat{\tau}_{j,l}\right), \quad (13)$$

where

$$\widehat{\rho}_{j,l} = \frac{\sum_{k=1}^K \mathbb{1}_{\{j,l \in V_k\}} \widehat{\rho}_{j_k, l_k}^{(k)}}{\sum_{k=1}^K \mathbb{1}_{\{j,l \in V_k\}}}, \quad \widehat{\tau}_{j,l} = \frac{\sum_{k=1}^K \mathbb{1}_{\{j,l \in V_k\}} \widehat{\tau}_{j_k, l_k}^{(k)}}{\sum_{k=1}^K \mathbb{1}_{\{j,l \in V_k\}}}, \quad (14)$$

and

$$\begin{aligned} \widehat{\rho}_{j,l}^{(k)} &= \frac{\sum_{i=1}^{n_k} (r_{i,j}^{(k)} - \bar{r}_j^{(k)})(r_{i,l}^{(k)} - \bar{r}_l^{(k)})}{\sqrt{\sum_{i=1}^{n_k} (r_{i,j}^{(k)} - \bar{r}_j^{(k)})^2 \sum_{i=1}^{n_k} (r_{i,l}^{(k)} - \bar{r}_l^{(k)})^2}}, \\ \widehat{\tau}_{j,l}^{(k)} &= \frac{2}{n_k(n_k - 1)} \sum_{1 \leq i < i' \leq n_k} \text{sign}((r_{i,j}^{(k)} - r_{i',j}^{(k)})(r_{i,l}^{(k)} - r_{i',l}^{(k)})). \end{aligned} \quad (15)$$

Assumption 1 (Weak distortion compared to signal). *We assume that the maximum off-diagonal distortion of the MAD_{GQ} solution is smaller than half the signal strength in the original precision matrix: $\delta < \frac{\nu}{2}$.*

Assumption 2. *For every node $i \in V$ with $N_{H_i}(i) \neq \emptyset$, we have that for every k such that $i \in V_k$, there exists at least one node $j \in V_k \setminus \{i\}$ that is $(H_i \cup \{j\})$ -connected to some node in $N_{H_i}(i)$.*

Assumption 3. *If $\delta_{i,\backslash i}^{(k)} \neq 0$, then there exists $j \neq i$ such that $0 < |\tilde{\Theta}_{ij}^{(k)}| < \delta$.*

Assumption 4 (Incoherence condition). Let $\Gamma = \widetilde{\Sigma} \otimes \widetilde{\Sigma}$, $S = \{(j, l) : \widetilde{\Theta}_{j,l} \neq 0\}$. We assume $\max_{e \in O \cap S^c} \|\Gamma_{e,S} \Gamma_{S,S}^{-1}\|_1 \leq 1 - \alpha$ for some $0 < \alpha \leq 1$.

Assumption 5 (Sufficient block measurements). The K blocks cover all nodes: $\cup_{k=1}^K V_k = [p]$, and at least one off-diagonal element: $|O| > p$.

Assumption 6 (Regularization parameter). $\Lambda_{j,l} = \frac{C_0}{\alpha} \sqrt{\frac{\log p}{\min_k n_k}}$ for all $(j, l) \in O$ and some universal constant $C_0 > 0$.

Theorem 1. Suppose that Assumptions 1-6 hold, and there exist at least one edge in the graph encoded by Θ and $\widetilde{\Theta}$: $d, \widetilde{d} > 2$. Then we have the following guarantees for Algorithm 1, with probability at least $1 - \sum_k p_k^{-10}$:

- **Exact recovery in O .** If

$$n_k > \left[\frac{C_0}{4} \kappa_{\widetilde{\Gamma}} \left(1 + \frac{8}{\alpha} \right) \left(\left(\frac{\nu}{2} - \delta \right)^{-1} + 3 \left(1 + \frac{8}{\alpha} \right) (\kappa_{\widetilde{\Sigma}} + \kappa_{\widetilde{\Sigma}}^3 \kappa_{\widetilde{\Gamma}}) \widetilde{d} \right) \right]^2 \log p_k, \quad (16)$$

$\delta + \varepsilon_1 \leq \tau_1 < \nu - \delta - \varepsilon_1$, where $\varepsilon_1 = \frac{C_0}{4} \kappa_{\widetilde{\Gamma}} (1 + \frac{8}{\alpha}) \max_k \sqrt{\frac{\log p_k}{n_k}}$, then $\widehat{E}_O = E_O$.

- **Minimal superset recovery in O^c .** If

$$n_k > C_0 \kappa_{\widetilde{\Gamma}}^2 \left(1 + \frac{8}{\alpha} \right)^2 \left[\frac{9\widetilde{\kappa}^4}{4\psi^2} + \frac{1}{4\lambda_{\min}(\widetilde{\Theta})^2} \right] \min\{p + \widetilde{s}, \widetilde{d}^2\} \log p_k, \quad (17)$$

$\varepsilon_2 \leq \tau_2 < \psi - \varepsilon_2$, $\delta - \varepsilon_2 < \tau_1 \leq \nu - \varepsilon_2$, where $\varepsilon_2 = \frac{3C_0}{4} \kappa_{\widetilde{\Gamma}} (1 + \frac{8}{\alpha}) \widetilde{\kappa}^2 \min\{\sqrt{p + \widetilde{s}}, \widetilde{d}\} \max_k \sqrt{\frac{\log p_k}{n_k}}$, then $\widehat{E}_{O^c} = \mathcal{S}_{\text{off}}$.

Proof of Theorem 1. First of all, we note that a population version of Theorem 1 has been proved in (Vinci et al., 2019) (see Theorem 3.1 and Theorem 3.4), which shows the exact edge recovery in O and minimal superset recovery in O^c based on thresholding $\widetilde{\Theta}$ and $\widetilde{\Theta}^{(k)}$. Our proof of Theorem 1 mainly involves applying the population results in (Vinci et al., 2019) and some new estimation error bounds for $\|\widehat{\widetilde{\Theta}} - \widetilde{\Theta}\|_\infty$ and $\|\widehat{\widetilde{\Theta}}^{(k)} - \widetilde{\Theta}^{(k)}\|_\infty$.

In particular, when Assumptions 1-3 hold, (Vinci et al., 2019) shows that

$$E_O = \{(i, j) \in O : |\widetilde{\Theta}_{i,j}| > t\}, \quad \forall \delta \leq t \leq \nu - \delta, \quad (18)$$

and for any $\delta \leq t \leq \nu$,

$$\mathcal{S}_{\text{off}} = O^c \cap (W_t \times W_t), W_t = \{i \in V : \forall k \text{ s.t. } i \in V_k, \exists j \neq i, 0 < |\widetilde{\Theta}_{ij}^{(k)}| < t\}. \quad (19)$$

On the other hand, the following two theorems show the proximity between $\widehat{\widetilde{\Theta}}$ and $\widetilde{\Theta}$, $\widehat{\widetilde{\Theta}}^{(k)}$ and $\widetilde{\Theta}^{(k)}$:

Theorem 2. Suppose that Assumptions 4 and 5 hold, $\Lambda_{j,l} = \frac{C_0}{\alpha} \sqrt{\frac{\log p}{\min_k n_k}}$ for all $(j, l) \in O$ and some universal constant $C_0 > 0$, and there exist at least one edge in the graph encoded by Θ and $\widetilde{\Theta}$: $d, \widetilde{d} > 2$. If for all $1 \leq k \leq K$,

$$n_k \geq \left[\frac{3C_0}{4} \left(1 + \frac{8}{\alpha} \right)^2 (\kappa_{\widetilde{\Sigma}} \kappa_{\widetilde{\Gamma}} + \kappa_{\widetilde{\Sigma}}^3 \kappa_{\widetilde{\Gamma}}^2) \right]^2 \widetilde{d}^2 \log p_k,$$

then with probability at least $1 - \sum_{k=1}^K p_k^{-10}$, $\widehat{\widetilde{\Theta}}$ defined in (4) satisfies

$$\|\widehat{\widetilde{\Theta}} - \widetilde{\Theta}\|_\infty \leq \frac{C_0}{4} \kappa_{\widetilde{\Gamma}} (1 + \frac{8}{\alpha}) \max_k \sqrt{\frac{\log p_k}{n_k}}.$$

Theorem 3. *Suppose all conditions in Theorem 2 hold. In addition, if for $1 \leq k \leq K$,*

$$n_k \geq \frac{C_0 \kappa_{\tilde{\Gamma}}^2 (1 + \frac{8}{\alpha})^2}{4 \lambda_{\min}(\tilde{\Theta})^2} \min\{p + \tilde{s}, \tilde{d}^2\} \log p_k,$$

then for any $1 \leq k \leq K$,

$$\|\widehat{\tilde{\Theta}}^{(k)} - \tilde{\Theta}^{(k)}\|_{\infty} \leq \frac{3C_0 \tilde{\kappa}^2 \kappa_{\tilde{\Gamma}} (1 + \frac{8}{\alpha})}{4} \min\{\sqrt{p + \tilde{s}}, \tilde{d}\} \max_k \sqrt{\frac{\log p_k}{n_k}}$$

holds with probability at least $1 - \sum_{k=1}^K p_k^{-10}$.

When the sample size condition (16) holds, the conditions in Theorem 2 are all satisfied, and hence $\|\widehat{\tilde{\Theta}} - \tilde{\Theta}\|_{\infty} \leq \varepsilon_1$ defined in Theorem 1. Thus when $\delta + \varepsilon_1 \leq \tau_1 \leq \nu - \delta - \varepsilon_1$,

$$\widehat{E}_O = \{(i, j) \in O : i \neq j, |\widehat{\tilde{\Theta}}_{i,j}| > \tau_1\} \subset \{(i, j) \in O : i \neq j, |\tilde{\Theta}_{i,j}| > \delta\} = E_O,$$

and

$$\widehat{E}_O \supset \{(i, j) \in O : i \neq j, |\tilde{\Theta}_{i,j}| > \tau_1 + \varepsilon_1\} \supset \{(i, j) \in O : i \neq j, |\tilde{\Theta}_{i,j}| > \nu - \delta\} = E_O.$$

The sample size condition (16) also ensures that $\nu - \delta - \varepsilon_1 > \delta + \varepsilon_1$ so that the required range for τ_1 is not empty.

In addition, when the sample size condition (17) holds, all conditions in Theorem 3 are satisfied, and the range for τ_2 is not empty. Thus $\|\widehat{\tilde{\Theta}}^{(k)} - \tilde{\Theta}^{(k)}\|_{\infty} \leq \varepsilon_2$. When $\varepsilon_2 \leq \tau_2 < \psi - \varepsilon_2$, $\delta - \varepsilon_2 < \tau_3 \leq \nu - \varepsilon_2$, the set $\widehat{W}_{\tau_2, \tau_3}$ defined in (6) satisfies

$$\begin{aligned} \widehat{W}_{\tau_2, \tau_3} &= \{i \in V : \forall k \text{ s.t. } i \in V_k, \exists j \neq i, \tau_2 < |\widehat{\tilde{\Theta}}_{i,j}^{(k)}| < \tau_3\} \\ &\subset \{i \in V : \forall k \text{ s.t. } i \in V_k, \exists j \neq i, 0 < |\tilde{\Theta}_{i,j}^{(k)}| < \nu\} \\ &= W_{\nu}, \end{aligned}$$

and

$$\begin{aligned} \widehat{W}_{\tau_2, \tau_3} &\supset \{i \in V : \forall k \text{ s.t. } i \in V_k, \exists j \neq i, \psi \leq |\tilde{\Theta}_{i,j}^{(k)}| \leq \delta - 2\varepsilon\} \\ &= \{i \in V : \forall k \text{ s.t. } i \in V_k, \exists j \neq i, 0 < |\tilde{\Theta}_{i,j}^{(k)}| < \delta\} \\ &= W_{\delta}, \end{aligned}$$

where the second line is due to Assumption 3. Therefore, combining these results with (19), one has $\widehat{E}_{O^c} = O^c \cap (\widehat{W}_{\tau_2, \tau_3} \times \widehat{W}_{\tau_2, \tau_3}) = \mathcal{S}_{\text{off}}$. \square

Proof of Theorem 2. Our proof follows similar ideas to the proof of Theorem 4.1 in (Vinci et al., 2019), while the main difference lies in the correlation matrix estimation. In particular, note that the population MAD_{GQ} solution $\tilde{\Theta}$ is the same as the one in (Vinci et al., 2019), computed from the population correlation matrix. While for the finite sample estimate $\widehat{\tilde{\Theta}}$ we defined in (4), it depends on the rank based correlation $\widehat{\Sigma}_O = \widehat{\Sigma}_O^{(\tau)}$ or $\widehat{\Sigma}_O^{(\rho)}$, instead of the sample covariance matrix.

However, one thing to note in the proof of Theorem 4.1 in (Vinci et al., 2019) is that we only care about the infinity-norm error bound $\|\widehat{\Sigma}_O - \Sigma_O\|_{\infty}$ instead of its specific form. The following lemma characterizes this error bound for both rank-based correlation estimates.

Lemma 1. *There exists a universal constant $C > 0$, such that as long as $n_k \geq C$ holds for all $1 \leq k \leq K$, with probability at least $1 - \sum_{k=1}^K p_k^{-10}$, $\widehat{\Sigma}_O^{(\rho)}$ and $\widehat{\Sigma}_O^{(\tau)}$ defined in (13) satisfy*

$$\|\widehat{\Sigma}_O^{(\rho)} - \Sigma_O\|_{\infty} \leq C \max_k \sqrt{\frac{\log p_k}{n_k}}, \quad \|\widehat{\Sigma}_O^{(\tau)} - \Sigma_O\|_{\infty} \leq C \max_k \sqrt{\frac{\log p_k}{n_k}}.$$

Lemma 1 is proved by applying Theorems 4.1 and 4.2 in (Liu et al., 2012) on each block k and a union bound over K blocks.

Inspired by Lemma 1, we specifically change the upper bound $\sigma(\bar{n}, p^b)$ in (Vinci et al., 2019) to $C \max_k \sqrt{\frac{\log p_k}{n_k}}$, which is an upper bound for $\|\widehat{\Sigma}_O - \Sigma_O\|_\infty$ with probability at least $1 - \sum_{k=1}^K p_k^{-10}$. Similar to (Vinci et al., 2019), we let $\lambda_{j,l} = \frac{C_0}{\alpha} \max_k \sqrt{\frac{\log p_k}{n_k}}$ with $C_0 = 8C$. Recognizing the fact that our sample size condition in Theorem 2 suggests

$$C \max_k \sqrt{\frac{\log p_k}{n_k}} \leq \left[6 \left(1 + \frac{8}{\alpha} \right)^2 \tilde{d} \max\{\kappa_{\widehat{\Sigma}} \kappa_{\widetilde{\Gamma}}, \kappa_{\widehat{\Sigma}}^3 \kappa_{\widetilde{\Gamma}}^2\} \right]^{-1},$$

we can follow the same arguments as in (Vinci et al., 2019), and eventually show that

$$\{(j, l) : \widehat{\Theta}_{j,l} \neq 0\} \subset \{(j, l) : \widetilde{\Theta}_{j,l} \neq 0\}, \quad (20)$$

and

$$\|\widehat{\Theta} - \widetilde{\Theta}\|_\infty \leq \frac{C_0}{4} \kappa_{\widetilde{\Gamma}} \left(1 + \frac{8}{\alpha} \right) \max_k \sqrt{\frac{\log p_k}{n_k}},$$

with probability at least $1 - \sum_{k=1}^K p_k^{-10}$. \square

Proof of Theorem 3. To prove Theorem 3, we make use of Lemma C.2 and Lemma C.3 in (Vinci et al., 2019), which bounds the entrywise error bounds of Schur complements as a function of the error of full matrices. For completeness, here we restate these two lemmas.

Lemma 2 (Lemma C.2 in (Vinci et al., 2019)). *Let $X, Y \in \mathbb{R}^{p \times p}$ be positive definite matrices. Then, for any nonempty set $A \subset [p]$,*

$$\|X/X_{A^c A^c} - Y/Y_{A^c A^c}\|_\infty \leq \frac{\lambda_{\max}(X) \lambda_{\max}(Y)}{\lambda_{\min}(X) \lambda_{\min}(Y)} \|X - Y\|_2 \quad (21)$$

where $X/X_{A^c A^c} = X_{AA} - X_{AA^c} (X_{A^c A^c})^{-1} X_{A^c A}$ is the Schur Complement of the block $A^c \times A^c$ of the matrix X , $\lambda_{\min}(X)$ and $\lambda_{\max}(X)$ are the smallest and the largest eigenvalues of X .

Lemma 3 (Lemma C.3 in (Vinci et al., 2019)). *For any $p \times p$ symmetric matrix X with max row-degree smaller than or equal to d , we have*

$$\|X\|_2 \leq \min(\sqrt{\|X\|_0}, d) \|X\|_\infty \quad (22)$$

where $\|X\|_2$ is the spectral norm, $\|X\|_0 := |\{(i, j) : X_{ij} \neq 0\}|$, and $\|X\|_\infty$ is the max norm.

As has been shown in the proof of Theorem 2, under appropriate conditions, with probability at least $1 - \sum_{k=1}^K p_k^{-10}$, the support set of $\widehat{\Theta}$ is a subset of the support set of $\widetilde{\Theta}$; and $\|\widehat{\Theta} - \widetilde{\Theta}\|_\infty \leq \frac{C_0}{4} \kappa_{\widetilde{\Gamma}} \left(1 + \frac{8}{\alpha} \right) \max_k \sqrt{\frac{\log p_k}{n_k}}$. Therefore, by applying Lemma 2, we have

$$\|\widehat{\Theta}^{(k)} - \widetilde{\Theta}^{(k)}\|_\infty \leq \frac{\lambda_{\max}(\widetilde{\Theta}) \lambda_{\max}(\widehat{\Theta})}{\lambda_{\min}(\widetilde{\Theta}) \lambda_{\min}(\widehat{\Theta})} \|\widehat{\Theta} - \widetilde{\Theta}\|_2, \quad (23)$$

and an application of Lemma 3 leads to

$$\begin{aligned} \|\widehat{\Theta} - \widetilde{\Theta}\|_2 &\leq \min\{\sqrt{p + \tilde{s}}, \tilde{d}\} \|\widehat{\Theta} - \widetilde{\Theta}\|_\infty \\ &\leq \frac{C_0}{4} \kappa_{\widetilde{\Gamma}} \left(1 + \frac{8}{\alpha} \right) \min\{\sqrt{p + \tilde{s}}, \tilde{d}\} \max_k \sqrt{\frac{\log p_k}{n_k}} \\ &\leq \frac{1}{2} \lambda_{\min}(\widetilde{\Theta}), \end{aligned}$$

where the last line is due to the sample size condition in Theorem 3. Hence $\lambda_{\max}(\widehat{\Theta}) \leq \lambda_{\max}(\widetilde{\Theta}) + \|\widehat{\Theta}^{(k)} - \widetilde{\Theta}^{(k)}\|_2 \leq \frac{3}{2}\lambda_{\max}(\widetilde{\Theta})$, and $\lambda_{\min}(\widehat{\Theta}) \geq \lambda_{\min}(\widetilde{\Theta}) - \|\widehat{\Theta}^{(k)} - \widetilde{\Theta}^{(k)}\|_2 \geq \frac{1}{2}\lambda_{\min}(\widetilde{\Theta})$. Combining these bounds for $\lambda_{\max}(\widehat{\Theta})$, $\lambda_{\min}(\widehat{\Theta})$, $\|\widehat{\Theta}^{(k)} - \widetilde{\Theta}^{(k)}\|_2$, with (23), we have

$$\|\widehat{\Theta}^{(k)} - \widetilde{\Theta}^{(k)}\|_2 \leq \frac{3C_0}{4} \kappa_{\Theta}^2 \kappa_{\widetilde{\Gamma}} (1 + \frac{8}{\alpha}) \min\{\sqrt{p + \widetilde{s}}, \widetilde{d}\} \max_k \sqrt{\frac{\log p_k}{n_k}}.$$

□

Proof of Lemma 1. Firstly, we note that our rank-based correlation matrices $\widehat{\Sigma}^{(\rho)}$ and $\widehat{\Sigma}^{(\tau)}$ are computed in three steps: we compute the rank statistics, Kendall's tau and Spearman's rho, for each block as in (15); we then combine the results of K blocks by taking an average on the overlapping part; finally, two sine transformations are applied entrywise on the combined rank statistics as in (13). In the following, we will prove the error bounds following the same three steps, and leverage similar ideas from the proof of Theorems 4.1 and 4.2 in (Liu et al., 2012).

In the first step, we note that for $1 \leq k \leq K$, $\widehat{\rho}_{j,l}^{(k)}$ and $\widehat{\tau}_{j,l}^{(k)}$ are computed as the standard Spearman's rho and Kendall's tau from the data $X^{(k)}$ of the k th block, and hence we can apply the Hoeffding's inequality for U-statistics as in the proof of Theorems 4.1 and 4.2 in (Liu et al., 2012):

$$|\widehat{\rho}_{j,l}^{(k)} - \mathbb{E}\widehat{\rho}_{j,l}^{(k)}| \leq C \sqrt{\frac{\log p_k}{n_k}}, \quad |\widehat{\tau}_{j,l}^{(k)} - \mathbb{E}\widehat{\tau}_{j,l}^{(k)}| \leq C \sqrt{\frac{\log p_k}{n_k}}, \quad (24)$$

for $j, l \in [p_k]$ and a universal constant $C > 0$, with probability at least $1 - p_k^{-10}$. Here, the exponent -10 can also be changed by any negative constant $-c$, as long as $C > 0$ in the upper bound in (24) is chosen appropriately. By the definition of $\widehat{\rho}$ and $\widehat{\tau}$ in (14) and a union bound over $1 \leq k \leq K$, we know that with probability at least $1 - \sum_{k=1}^K p_k^{-10}$,

$$|\widehat{\rho}_{j,l} - \mathbb{E}\widehat{\rho}_{j,l}| \leq C \max_k \sqrt{\frac{\log p_k}{n_k}}, \quad |\widehat{\tau}_{j,l} - \mathbb{E}\widehat{\tau}_{j,l}| \leq C \max_k \sqrt{\frac{\log p_k}{n_k}}.$$

To transform the bounds above to the bounds for the estimated correlation matrices, we note that $\Sigma_{j,l} = \sin(\frac{\pi}{2}\mathbb{E}\widehat{\tau}_{j,l})$, $\widehat{\Sigma}_{j,l}^{(\tau)} = \sin(\frac{\pi}{2}\widehat{\tau}_{j,l})$, and the Lipschitz property of the sine function implies

$$|\widehat{\Sigma}_{j,l}^{(\tau)} - \Sigma_{j,l}^{(\tau)}| \leq \frac{\pi}{2} |\widehat{\tau}_{j,l} - \mathbb{E}\widehat{\tau}_{j,l}|. \quad (25)$$

While for $\widehat{\Sigma}^{(\rho)}$, as has been shown in the proof of Theorem 4.1 in (Liu et al., 2012),

$$\mathbb{E}\widehat{\rho}_{j_k, l_k}^{(k)} = \frac{6}{\pi} \arcsin\left(\frac{\Sigma_{j,l}}{2}\right) + \frac{6}{\pi(n_k + 1)} \left(\arcsin(\Sigma_{j,l}) - 3 \arcsin\left(\frac{\Sigma_{j,l}}{2}\right) \right).$$

Denote by $a_{j,l}^{(k)}$ the excess error term:

$$a_{j,l}^{(k)} = \mathbb{E}\widehat{\rho}_{j_k, l_k}^{(k)} - \frac{6}{\pi} \arcsin\left(\frac{\Sigma_{j,l}}{2}\right) = \frac{6}{\pi(n_k + 1)} \left(\arcsin(\Sigma_{j,l}) - 3 \arcsin\left(\frac{\Sigma_{j,l}}{2}\right) \right),$$

then we know that $|a_{j,l}^{(k)}| \leq \frac{12}{n_k + 1}$. Thus, by the definition of $\widehat{\rho}$ in (14),

$$\mathbb{E}\widehat{\rho}_{j,l} = \frac{6}{\pi} \arcsin\left(\frac{\Sigma_{j,l}}{2}\right) + \frac{\sum_{k=1}^K \mathbb{1}_{\{j,l \in V_k\}} a_{j,l}^{(k)}}{\sum_{k=1}^K \mathbb{1}_{\{j,l \in V_k\}}},$$

and

$$\begin{aligned} |\widehat{\Sigma}_{j,l}^{(\rho)} - \Sigma_{j,l}^{(\rho)}| &= \left| 2 \sin\left(\frac{\pi}{6}\widehat{\rho}_{j,l}\right) - 2 \sin\left(\frac{\pi}{6}\mathbb{E}\widehat{\rho}_{j,l} - \frac{\sum_k \mathbb{1}_{\{j,l \in V_k\}} a_{j,l}^{(k)}}{\sum_k \mathbb{1}_{\{j,l \in V_k\}}}\right) \right| \\ &\leq \frac{\pi}{3} \left(|\widehat{\rho}_{j,l} - \mathbb{E}\widehat{\rho}_{j,l}| + \frac{12}{\min_k n_k + 1} \right). \end{aligned} \quad (26)$$

Therefore, combining (26), (25), (24), the proof of Lemma 1 is completed. □